Karlsruhe Institute of Technology

Praktikum: P4   Gruppe: 22   ■ **Mo**   ☐ **Mi**   **WS20/21**

Zutreffendes bitte ausfüllen

Namen: Paul Filip   useba[at]student.kit.edu

Namen: Janic Beck

Versuch: Comptoneffekt

Betreuer: Roxanne Turcotte   Durchgeführt am: 16.11.20

Wird vom Betreuer ausgefüllt.

1. Abgabe am: _____

Rückgabe am: _____   Kommentar:

2. Abgabe am: _____

Ergebnis: + / 0 / - Handzeichen: _____

Datum: _____   Kommentar:

Contents

1. Theory & Preparation

1.1 Compton scattering

Consider the scenario of a high-energy photon interacting with an unbound electron as shown in Figure 1.1a. To describe this process we choose a coordinate frame where the electron is at rest with respect to us. In the experiments to be presented in this report such a coordinate frame conveniently is the lab frame. Furthermore, we employ natural units, $\epsilon_0 = \hbar = c = 1$.
From the conservation of energy and impluse a theoretical description of this process can be constructed based on the inital and final energies of both particles.

$$E_{\gamma,i} + \underbrace{E_{e,i}}_{=0} = E_{\gamma,f} + E_{e,f}$$

$$p_{\gamma,i} + \underbrace{p_{e,i}}_{=0} = p_{\gamma,f} + p_{e,f}$$

From the above relations an expression for the energy of the photon after interacting with the electron can be obtained as lined out in [**?**]. The expression reads

$$E_{\gamma,f} = \frac{E_{\gamma,i}}{1 + \frac{E_{\gamma,i}}{m_e}(1 - \cos\theta)}, \tag{1.1}$$

where θ defines the angle spanned between the incident photon and its path post scattering. It follows that the electron gains energy from the interaction.

$$E_{e,f} = E_{\gamma,i} - E_{\gamma,f} = E_{\gamma,f} \cdot \frac{E_{\gamma,i}}{m_e} \cdot (1 - \cos\theta). \tag{1.2}$$

The measureable change in the photons wavelength $\lambda = \frac{hc}{E_\gamma}$ due to the interaction is called the **Compton effect**. The underlaying elastic scattering of photons and unbound electrons is consequently labelled **Compton scattering**. Alongside Photoionisation and Pair production it represents one of the important processes by which electromagnetic radiation interacts with matter.

The physical characteristics of Compton scattering, namely its cross section and the resulting distribution of electron energies will be discused in the following section 1.2 and section 1.3.
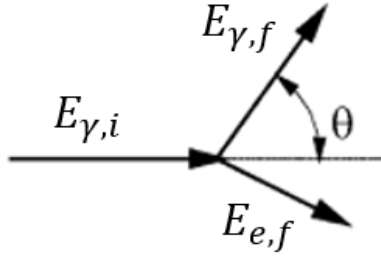
(a) **Scattering kinematics**
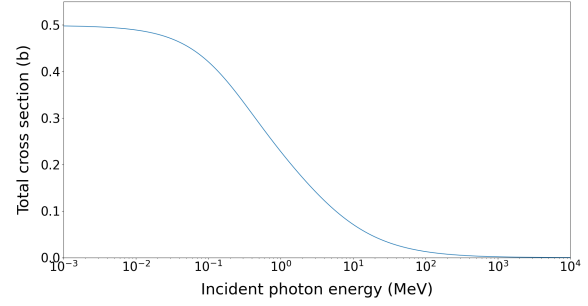
(b) **Total cross section**

(a) A high energy photon scatters off a free electron at rest. The defining variables to describe this process are given by $E_{\gamma,i}$ and θ. Figure adapted with changes from [**?**]. (b) The total cross section for compton scatter as a function of the incident photon energy. Roughly constant for low-energy photons, the total cross section drops off for higher energies.

1.2 Cross section

Compton scattering is the dominating effect by which photons with an energy between $100\,\text{keV}$ and $10\,\text{MeV}$ interact with matter [**?**]. A theoretical description of the processes cross section is given by the **Klein-Nishina formula** (KN), which gives the differential cross section of Compton scattering.

$$\frac{\mathrm{d}\sigma}{\mathrm{d}\Omega}\,_{\text{KN}} = \frac{\alpha^2}{2m_e}\left(\frac{E_{\gamma,f}}{E_{\gamma,i}}\right)^2\left[\frac{E_{\gamma,f}}{E_{\gamma,i}} + \frac{E_{\gamma,i}}{E_{\gamma,f}} - \sin^2\theta\right] \tag{1.3}$$

Integrating over all solid angles and defining $x = \frac{E_{\gamma,i}}{m_e}$, one obtains the total cross section.

$$\sigma_{\text{tot.}} = \int \frac{\mathrm{d}\sigma}{\mathrm{d}\Omega}\,\mathrm{d}\Omega = \frac{\pi\alpha^2}{m_e^2}\frac{1}{x^3}\left(\frac{2x(2+x(1+x)(8+x))}{(1+2x)^2} + ((x-2)x - 2\log(1+2x))\right) \tag{1.4}$$

In the low-energy limit of $x \ll 1$ Equation 1.4 simplifies to a constant called the **Thomson cross section**, whereas in the high-energy limit $x \to \infty$ we expand in x to find that the cross section vanishes. This behaviour can also be seen in Figure 1.1b.

$$x \ll 1: \qquad \sigma_{\text{tot.}} = \frac{8\pi\alpha^2}{m_e^2} \approx 0.6652\,\text{b}$$

$$x \longrightarrow \infty: \qquad \sigma_{\text{tot.}} = \frac{\pi\alpha^2}{xm_e^2}\left(\frac{1}{2} + \log 2x\right)$$

Naively, one would therefore expect Compton scattering to be an important process for low to intermediate energy ranges of the electromagnetic spectrum, where the cross section $\sigma_{\text{tot.}}$ is non-negligible. This is however not the case. Various other processes such as the photoelectric effect or Rayleigh scattering dominate the low energy regime and render Compton scattering only a fringe case. With higher photon energies, the cross section for the aforementioned processes drop off, and increase the importance of Compton scattering for gammas carrying an energy of $100\,\text{keV}$ up to $10\,\text{MeV}$.
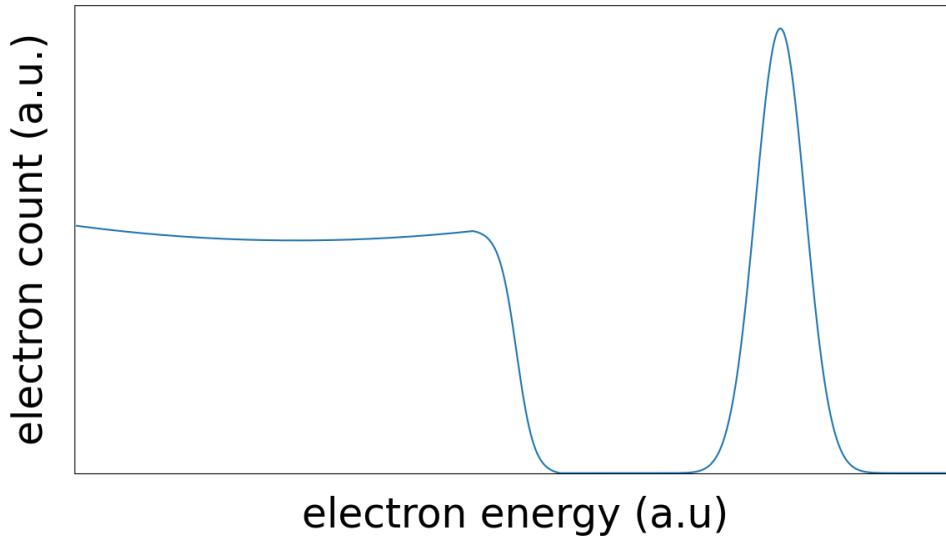
Figure 1.2: An idealised Compton spectrum. A relatively constant flux of electrons is measured up to an energy of $E_{\max}$, where the spectrum sharply drops off. At the high-energy end of the spectrum a gaussian shaped photopeak is visible.

1.3 Compton spectrum

Without knowing anything about the distribution of energies or deflection angles of the scattered electrons, by examining Equation 1.2 it can already be established that the energy the electron gains from the interaction is directly proportional to $(1 - \cos\theta)$, or in other words, by how much the photon is scattered away from its original path. It follows that for $\theta = 180°$ the electron gains a maximum energy of

$$E_{\max} = \frac{E_\gamma}{1 + \frac{m_e c^2}{E_\gamma}}. \tag{1.5}$$

Since the photon physically cannot dump more energy by this process, a sharp drop in the Compton spectrum at $E_{\max}$ is expected. This characteristic drop-off is commonly called the **Compton edge**. Energetically lower than this cutoff lays the **Compton continuum**. Over a wide range of energies that correspond to scattering angles $\theta \in [0°, 180°]$ the flux of electrons remains approximately constant. This follows directly from Equation 1.3. While the Compton continuum is symmetric in the idealised spectrum given in Figure 1.2, this is only really valid in the low energy limit. For higher photon energies forward scattering becomes much more probable. An example of this is given in section 2.3.

Lastly, an idealised Compton spectrum will also display a characteristic **photopeak**. This photopeak is caused by photons directly interacting with detector material via the photoelectric effect. In this case, the entire energy of the photon (which is generally known a priori) is dumped inside the detector. It is therefore a helpful reference point for calibrations, albeit not being part of the Compton spectrum itself.

The measured Compton spectrum discussed in chapter 2 may display several other characteristics such as a prominent X-ray line or a backscatter peak. These properties are dependant on the experimental setup. As such they will - if needed - be discussed in the appropriate sections of chapter 2.

2. Experiment & Evaluation

2.1 Experimental setup

The multi channel analyser (MCA) consists of a $20.43\,\mathrm{cm}^2$ large NaJ scintilling crystal as well as a photo-multiplier (PMT) useful for signal amplification. A readout chip allows for the digital treatmeant of measurement data. The detector is placed on metallic guiding rails that allow the scintillator to be placed at various positions on a circle around a plastic pedestal. A small $1\,\mathrm{cm} \times 1\,\mathrm{cm}$ target can be placed on the pedestal such that it is located in the beam path of a high-energy γ-source. The angle enclosed by the beam path and a line connecting scintillator detector with the target pedestal defines the scattering angle θ.

2.2 Calibration of a multichannel analyser

As a first task the MCA needs to be calibrated so that measured channel numbers of an event can be related to the energy of the particles that caused it. The presented calibration is fourfold. In seperate measurements the radionuclides Cobalt-57, and -60, as well as Sodium-22, and Caesium-137 are placed in front of the NaJ-scintillator. Their γ-spectrum is measured for $300\,\mathrm{s}$. The resulting distribution of observed events across the different measuring channels is depicted in Figure 2.1. The interesting parts of the spectra are the gaussian shaped sections located at the tail ends. They represent the photopeaks discussed briefly in section 1.3.

Equipped with theoretical knowledge of the radioactive processes, one can compare the measured channel with the expected energy of a nuclear transition to establish a linear connection between the two. For a more solid result this calibration is done simultanously for all measured radionuclides. A linear regression over all reference points then allows a quantitative analysis of measurement results. Below listed in Table 2.1 are the different observed radioactive transitions, their characteristic transition energies, as well as the channel they were observed in by the MCA, the last column holds information about the location of a guassian fit applied to the signal. In the bottom plot of Figure 2.1 these results are furthermore visualised.

As can be seen both in the plot as well as the table, a calibration for the photopeaks of ^{60}Co are not conducted. Extrapolating from the location of other photopeaks the characteristic points of the ^{60}Co γ-spectrum should be located around channels #195 and #223. This can however not be experimentally verified. A reasonable analysis is not possible, as the photopeaks are - provided the presented methodology is sound - far too faint. This can perhaps be prevented in future lab assignments by gathering more data of the ^{60}Co spectrum.

In any case, a linear model that connects channel number $\mathcal{C}$ to a particle energy E is obtained. They can be related to each other via Equation 2.1 that is presented below.
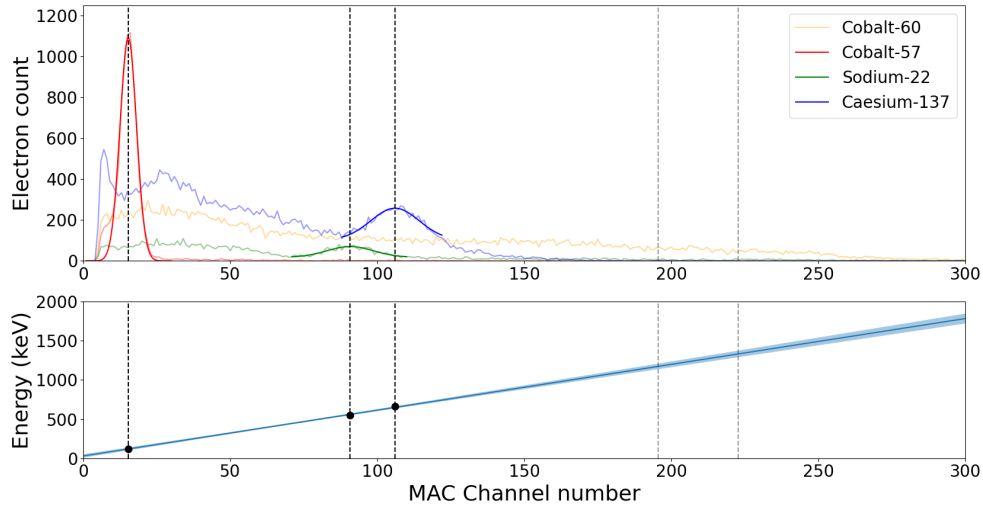
Figure 2.1: The gamma spectra of various radionuclides as measured by the MCA is depicted in the upper plot. A Gaussian fit hightlights the characteristic photopeaks for each (except Co-60, see text) measurement. The lower plot sets the measured channel numbers into context with the energies of the observed transitions. A linear model that connects MCA channel number with an energy is established.

Table 2.1: MCA energy calibration parameters

Transition	Energy (keV)	mes. channel	fit channel
^{57}Co $\rightarrow$ ^{57}Fe	122.061 [?]	16	15.3(1)
^{22}Na $\rightarrow$ ^{22}Ne	546.544 [?]	91	90.8(4)
^{137}Cs $\rightarrow$ ^{137m}Ba	661.659 [?]	108	106.0(3)
^{60}Co $\rightarrow$ ^{60}Ni*	1173.200 [?]	-	see text
^{60}Ni* $\rightarrow$ ^{60}Ni	1332.000 [?]	-	see text

$$E(\mathcal{C}) = \underbrace{(5.8 \pm 0.3)\,\text{keV}}_{a} \cdot \mathcal{C} + \underbrace{(30.2 \pm 22.0)\,\text{keV}}_{b} \tag{2.1}$$

Albeit only three of the four radionuclides can be used effectively for a calibration, the results nevertheless seem promising. A quick check regarding the goodness of fit finds a reduced $\chi_\nu^2 \approx 0.97$, indicating that the model conforms with observations to reasonable accuracy. This accuracy $\Delta E(\mathcal{C})$ can then be quantified using the covariance matrix $\text{COV}(a, b)$, estimated by the fitting algorithm, as well as the gradient ∇E, which can easily be calculated by hand.

$$\text{COV}(a, b) = \begin{bmatrix} 0.0736 & -5.2014 \\ -5.2014 & 483.5527 \end{bmatrix}, \qquad \nabla E = \begin{pmatrix} \mathcal{C} \\ 1 \end{pmatrix}.$$

$$\Delta E(\mathcal{C}) = \sqrt{(\nabla E)^T \, \text{COV}(a, b) \, \nabla E}. \tag{2.2}$$

It is expected that the uncertainties in $E(\mathcal{C})$ grow large for energies located far away from the calibration points. This is espically the case for high scattering angles.

2.3 Differential cross section

As a second task, the validity of the Klein-Nishina formula presented in Equation 1.3 is tested. For this purpose, the spectrometer is placed at various angles relative to the beam path. For every angle two measurements of $300\,\text{s}$ each are taken. One measurement with a cylindrical aluminum target in the beam path that allows for Compton scattering. The second measurement is conducted without any target and will help quantify the background noise measured by the spectrometer. The resulting distribution of electron energies is shown in Figure 2.2 for all measurements.

Before processing the data further, the abnormally high counts for the measurements at 0 and 10 degrees need to be adressed. The gamma spectra look identical whether a target is placed in the beam path or not. In this case γ's can directly propagate from the ^{137}Cs-source to the scintillating crystal due to the low deflection angle of the experimental setup. It is not the Compton spectrum that is measured at these angles, but rather the flux ϕ_0 of the γ source. The two measurements have to be discarded in the following analysis.

Furthermore, the detector quantum efficiency ϵ has to be evaluated. For this purpose a second order polynomial is fitted to Plot 7.10 (p.134) in [**?**]. The parameters of the best fit result are given below.

$$\epsilon(E) = aE^2 + bE + c$$
$$a = (1.77 \pm 0.10) \times 10^{-6} \, \frac{1}{\text{MeV}^2}$$
$$b = (-2.340 \pm 0.087) \times 10^{-3} \, \frac{1}{\text{MeV}}$$
$$c = 1.252 \pm 0.017$$

In the subsequent analysis, the counts for each measured channel are normalised with respect to the detector efficiency at the energy corresponding to the specific channel (see Equation 2.1). The corrected count for each channel is given as $n_{\mathcal{C},\text{corr}} = \frac{n_{\mathcal{C}}}{\epsilon(E(\mathcal{C}))}$. All detector hits are then summed up and divided by the measurement length to get the
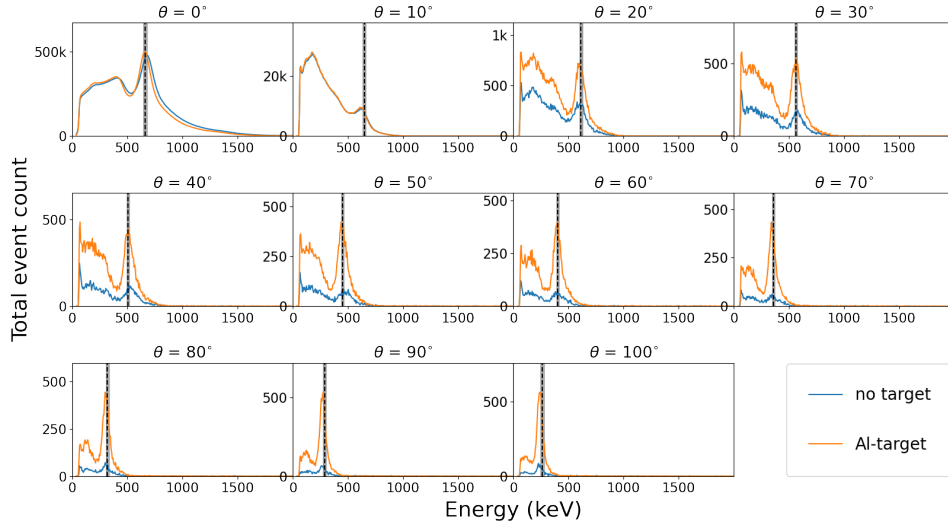
Figure 2.2: Raw number of events counted in every channel for each measured angle. The dashed black lines indicate the theoretical energy a photon has after undergoing compton scattering at an angle θ. The distance between signal peaks and this energy grows with increasing scattering angles. This is expected due to the imperfect calibration.

integrated rate R at one specific solid angle $\Delta\Omega$ and one specific scattering angle θ. From this, the differential cross section $\frac{\mathrm{d}\sigma}{\mathrm{d}\Omega}$ can be obtained as lined out in [?].

$$\frac{\mathrm{d}\sigma}{\mathrm{d}\Omega} = \frac{R(\Delta\Omega, \theta)_{\mathrm{Sig}} - R(\Delta\Omega, \theta)_{\mathrm{Bkg}}}{\Delta\Omega \cdot \phi_0 \cdot n_e}, \tag{2.3}$$

where $\Delta\Omega$ is the solid angle covered by the scintillator detecor as seen from the target position. ϕ_0 is the flux of photons hitting the target. n_e holds information about the number of scattering partners (i.e. electrons) available to a single photon. With information given in [?] their numerical value can be calculated as shown below. Note that in order to quantify errors in the mentioned variables, all information given by [?] is assumed to be exact.

$$\Delta\Omega = (0.011\,05 \pm 0.000\,00)\,\mathrm{sr}$$

$$\phi_0 = (4.956 \pm 0.290) \times 10^9 \,\frac{1}{\mathrm{m}^2\,\mathrm{s}}$$

$$n_e = (6.153 \pm 0.688) \times 10^{23}$$

Assuming a poissonian error $\Delta N = \sqrt{N}$ for each channel, as well as neglecting any possible correlation, Equation 2.3 holds an uncertainty ΔS, which propagates like

$$\Delta S = \sqrt{\left(\frac{\Delta R(\Delta\Omega, \theta)}{\Delta\Omega\phi_0 n_e}\right)^2 + \left(\frac{R(\Delta\Omega, \theta)}{\Delta\Omega\phi_0 n_e} \cdot (\frac{\Delta\phi_0}{\phi_0} + \frac{\Delta n_e}{n_e})\right)^2} \tag{2.4}$$

The results of this analysis are presented in Figure 2.3. They withstand the comparison to theoretical values given by Equation 1.3. Worrysome is however a constant offset by
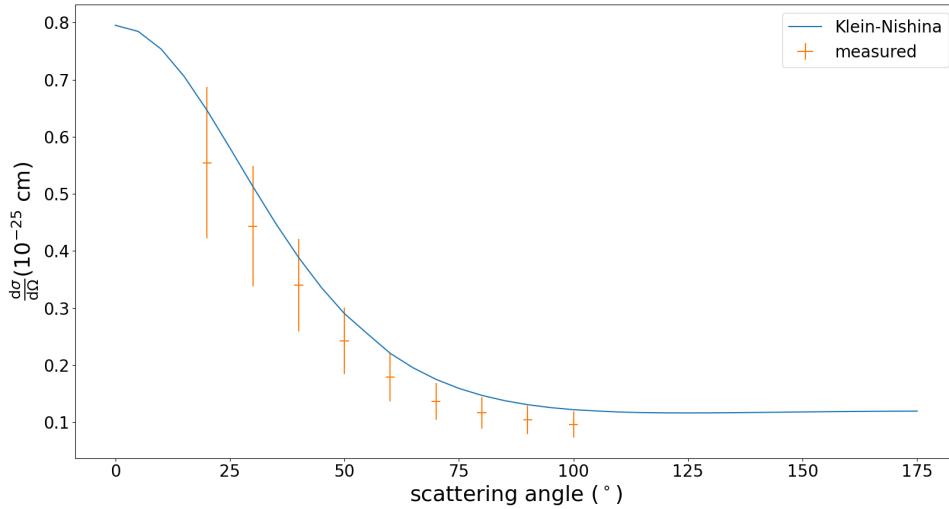
Figure 2.3: The experimentally measured differential cross section is compared to the theoretically predicted values given by the Klein-Nishina formula. While the gathered data is in good accordance with the theory, the measured values are offset by a constant. This indicates the presence of systematic errors.

which the measurements deviate from theoretical data. The offset indicates the presence of systematic errors in the experiment. One certain error source may be the imperfect energy-channel calibration discussed in section 2.2.

2.4 Energy shift & electron rest mass

In an attempt to estimate the rest mass of the electron, Equation 1.1 can be manipulated.

$$\frac{1}{E_{\gamma,f}} = \frac{1}{E_{\gamma,i}} + \frac{1}{m_e} \cdot (1 - \cos\theta). \tag{2.5}$$

According to Equation 2.5 the plot of $\frac{1}{E_{\gamma,f}}$ over $(1 - \cos\theta)$ should be a line with slope $\frac{1}{m_e}$ and intercept $\frac{1}{E_{\gamma,i}}$. A linear regression should be able to estimate m_e from the measurement data gathered in section 2.3.

The photon energy $E_{\gamma,f}$ post-scattering can be directly extracted from the location of the gaussian peaks present in the measured compton spectra. For the sake of a more solid analysis, a normal distribution is fitted to each peak. The results of these processes are listed in Table 2.2. The median of the best fit result is then taken as $E_{\gamma,f}$ in the subsequent discussion.

It has to be mentioned that the linear regression used to gather information about m_e only has one free parameter, the electron mass itself. The initial photon energy is manually set to the theoretical transition energy $661.659\,\text{keV}$ and assumed to be free of any errors. This is necessary to ensure a stable (and reasonably sensible) fit result. The analysis finds the best fit parameter

$$m_e = (459.72 \pm 6.00)\,\text{keV}, \tag{2.6}$$

which deviates from the literature value $(510.999\,\text{keV}\ [\textbf{?}])$ by about 10%. It does not lay within the uncertainty bounds of the "correct" value either. Possible reasons are an

Table 2.2: Calculated energy shift

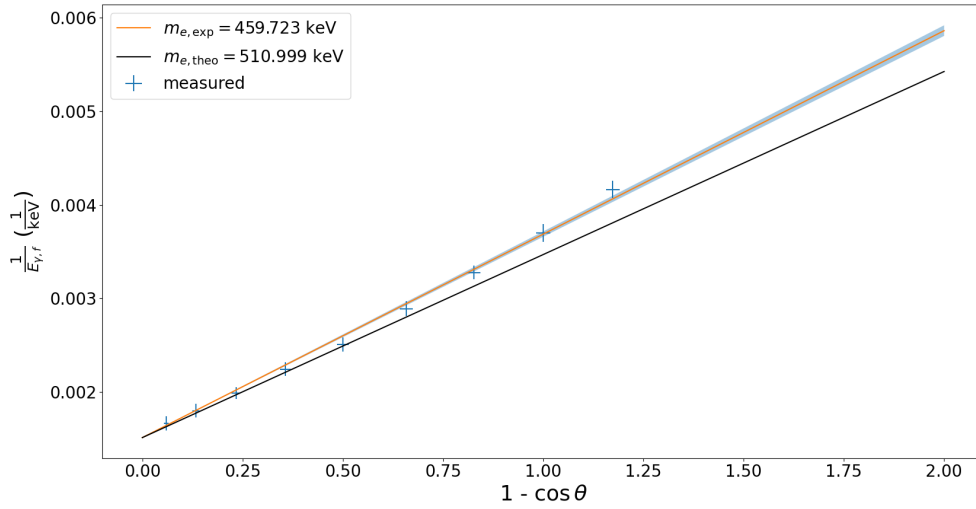| θ (°)	$1 - \cos\theta$	$E_{\gamma,f}$ (keV)	inv. (keV^{-1})
20	0.060	601.07 ± 2.76	0.0017 ± 0.0001
30	0.134	556.07 ± 2.29	0.0018 ± 0.0001
40	0.234	503.18 ± 1.68	0.0020 ± 0.0001
50	0.357	445.76 ± 1.44	0.0022 ± 0.0001
60	0.500	398.55 ± 1.21	0.0025 ± 0.0001
70	0.658	346.06 ± 0.97	0.0029 ± 0.0001
80	0.826	305.15 ± 0.69	0.0033 ± 0.0001
90	1.000	270.31 ± 0.68	0.0037 ± 0.0001
100	1.174	240.19 ± 0.53	0.0042 ± 0.0001

Figure 2.4: Comparison of the calculated linear model with literature values. Notable is the relatively small deviation from the literature value for small angles. This again hints at a poor energy calibration of the MCA.

underestimation of systematic errors in the energy calibration. Correlations between the respective measurements are also expected to play a part. The results of this analysis are visualised in Figure 2.4.

2.5 Z-dependency of differential cross section

Lastly, the differential cross section $\frac{d\sigma}{d\Omega}$ at one specific angle ($\theta = 20°$) is compared for different elements. Assuming Equation 1.3 holds for a photon scattering off a single electron, the cross section of the photon scattering off any electron inside an atom should scale like

$$\left(\frac{d\sigma}{d\Omega}\right)_{\text{Atom}} = Z \cdot \left(\frac{d\sigma}{d\Omega}\right)_{\text{electron}} \tag{2.7}$$

This espically implies that the quantity $\frac{R \cdot A}{\rho \cdot Z}$ connecting the measured event rate R with the material specific density ρ, atomic number Z, and atomic mass number A should be a

Table 2.3: Z dependance of R

Element	Z/A	$R \ (\frac{1}{s})$	$\frac{R \cdot A}{\rho \cdot Z}$ mol cm^3
Al	13/26.982	49.00±0.95	37.66±0.73
Fe	26/55.845	155.23±1.12	42.34±0.31
Cu	29/63.546	166.09±1.14	40.62±0.28
Pb	82/207.200	132.46±1.09	29.51±0.24

constant. This is tested by placing targets of the same geometry, but differing materials into the beam path. The number of events seen by the scintillator detector is counted for 300 s and treated as outlined in section 2.3 to obtain the interaction rate R. The results as well as reference data is listed in Table 2.3. As can be seen in the table, the quantity $\frac{R \cdot A}{\rho \cdot Z}$ is not constant. This cannot be attributed to a faulty energy calibration, as all systematic errors remain the same for these measurements and should cancel out upon comparison. The reason for the nonconformity is unclear and may be caused by untreated detector systematics.

The measured rate for the lead target is the most prominent outlier at a mean deviation of 30% relative to other measurements. This is most likely caused by the poor material quality of the lead target. Due to previous handling the top part of the lead target broke off. It therefore has a smaller geometry than all other targets. The measured rate is expected to drop accordingly.

2.6 Conclusion

Different aspects of Compton scattering were tested both qualitatively and quantitatively. While the results of the presented analysis are generally in good accordance with theoretical models of the process, several predictions, such as the rest mass of the electron, made by the model fail. One of the key things that can be improved in this report is the quality of the MCA calibration to measured energy. Allowing for more calibration points greatly improves the quality of the resulting fit.